nature communications

Article

https://doi.org/10.1038/s41467-024-52131-w

Effect of ion-specific water structures at metal surfaces on hydrogen production

Received: 13 November 2023

Accepted: 27 August 2024

Published online: 07 September 2024

Check for updates

Ye Tian[1,10] ✉, Botao Huang[2,3,10], Yizhi Song[1,4,10], Yirui Zhang[2,10], Dong Guan[1], Jiani Hong[1], Duanyun Cao[1], Enge Wang[1,5,6,7], Limei Xu[1,5,7] ✉, Yang Shao-Horn[2,8,9] ✉ & Ying Jiang[1,5,7] ✉

Water structures at electrolyte/electrode interfaces play a crucial role in determining the selectivity and kinetics of electrochemical reactions. Despite extensive experimental and theoretical efforts, atomic-level details of ion-specific water structures on metal surfaces remain unclear. Here we show, using scanning tunneling microscopy and noncontact atomic force microscopy, that we can visualize water layers containing alkali metal cations on a charged Au(111) surface with atomic resolution. Our results reveal that Li^+ cations are elevated from the surface, facilitating the formation of an ice-like water layer between the Li^+ cations and the surface. In contrast, K^+ and Cs^+ cations are in direct contact with the surface. We observe that the water network structure transitions from a hexagonal arrangement with Li^+ to a distorted hydrogen-bonding configuration with Cs^+. These observations are consistent with surface-enhanced infrared absorption spectroscopy data and suggest that alkali metal cations significantly impact hydrogen evolution reaction kinetics and efficiency. Our findings provide insights into ion-specific water structures on metal surfaces and underscore the critical role of spectator ions in electrochemical processes.

The microscopic structure of electrical double layer (EDL) between the electrode and electrolyte underpins a great importance, influencing both the selectivity and kinetics of numerous electrochemical reaction processes[1–5]. The Gouy–Chapman–Stern (GCS) model has served as the predominant framework for describing the EDL, which encompasses a Stern layer and a diffuse layer[6]. The Stern layer characterizes the arrangement/packing of water and ions on the surface, critically influencing mass transport to/from the interface and charge transfer processes[7–11]. However, this model, rooted in classical mean-field theory, overlooks the specific water orientation and ion arrangement at the molecular scale. Therefore, it struggles to interpret phenomena such as ion-specific effects[12–16], overcharging[17,18] and water orientational asymmetry[19,20]. Furthermore, alkali metal cations have been found to alter the interfacial solvation environment and electrochemically active sites. These modifications in turn impact the proton-coupled electron-transfer (PCET) barrier in hydrogen evolution reaction (HER)/hydrogen oxidation reaction (HOR) and the mass transport processes of oxidation reactions, varying with the different cations present[7,13,21,22].

Exploring molecular-level details of an EDL, from both experiment and theory, remains a formidable challenge. Various vibrational

[1]International Center for Quantum Materials, School of Physics, Peking University Beijing, P. R. China. [2]Electrochemical Energy Laboratory, Massachusetts Institute of Technology, 77 Massachusetts Avenue, Cambridge, MA, USA. [3]Research Laboratory of Electronics, Massachusetts Institute of Technology, 77 Massachusetts Avenue, Cambridge, MA, USA. [4]Department of Physics, Temple University, Philadelphia, Pennsylvania, USA. [5]Collaborative Innovation Center of Quantum Matter, Beijing, P. R. China. [6]Songshan Lake Materials Lab, Institute of Physics, CAS and School of Physics, Liaoning University, Shenyang, P. R. China. [7]Interdisciplinary Institute of Light-Element Quantum Materials and Research Center for Light-Element Advanced Materials, Peking University Beijing, P. R. China. [8]Department of Mechanical Engineering, Massachusetts Institute of Technology, 77 Massachusetts Avenue, Cambridge, MA, USA. [9]Department of Material Science and Engineering, Massachusetts Institute of Technology, 77 Massachusetts Avenue, Cambridge, MA, USA. [10]These authors contributed equally: Ye Tian, Botao Huang, Yizhi Song, Yirui Zhang. ✉e-mail: tianye420@pku.edu.cn; limei.xu@pku.edu.cn; shaohorn@mit.edu; yjiang@pku.edu.cn

spectroscopy[23–27] and diffraction techniques[28,29] have been employed to identify the EDL structure at electrode/electrolyte interfaces. In particular, advancements in surface enhanced vibrational spectroscopy, including surface enhanced Raman spectroscopy (SERS)[26,30] and surface enhanced infrared absorption spectroscopy (SEIRAS)[24,31,32], have enabled researchers to discern the dipole orientation and H-bonding structure of water molecules near the electrified interface. However, these techniques endure poor spatial resolution and the difficulty of spectral assignment. Recently, individual Na^+ hydrates, hydronium-water layers and alkali ion-water chains were successfully visualized by noncontact atomic force microscopy (AFM) with a carbon monoxide (CO)-terminated tip. This development opens up the possibility of probing interfacial ion-water interactions with atomic precision[33–36].

In this work, we investigated the extended network formed by different alkali metal cations and water molecules on a charged Au(111) surface in real space, which constitutes an ideal model system to understand the atomic structure at electrolyte/electrode interface. We were able to fabricate a sample with an ion concentration of ~10 M at the surface, corresponding to an effective bulk ion concentration of ~0.1 M[37] and resulting in a Stern layer thickness of ~6 Å[38]. Combining high-resolution scanning tunnelling microscopy (STM), AFM with CO-functionalized tips, and density functional theory (DFT) calculations, we deciphered the atomic structures of the cation-water networks on the Au(111) surface. These results showed that the water molecules were able to lift the Li^+ cations from the substrate, with the underlying water molecules forming an ordered hexagonal structure. In contrast, the Cs^+ and K^+ cations tend to adsorb on the substrate directly, disrupting the water structure. We also used SEIRAS to discern the water structure at the electrochemical solution/Au interface with varied cation species, which share similar features with our STM/AFM findings. Additionally, our HER analyzes suggest that the reaction efficiency is influenced by the cation species due to their impact on the interfacial water structure.

Results

Cs^+-water monolayer with distorted H-bonding network

The diverse cation-water structures were grown on the Au(111) surface by depositing alkali metal atoms at room temperature, followed by dosing water molecules at ~120 K. Since the alkali metal atoms have smaller work functions than the Au(111) surface, electrons will transfer from the alkali metal atoms to the Au substrate. This causes the alkali metal atoms to become cations and renders the Au(111) surface negatively charged, leading to electrostatic and dispersion interactions between the alkali metal cations and the Au substrate (Supplementary Text 1, Supplementary Figs. 1, 2). Additionally, owing to the Fermi-level nature of metal substrate, the charge transfer process from alkali metal atoms to the metal surfaces is a widely used method to simulate electrified interfaces with a net charge[26,39]. Figure 1a shows STM images of a 2D Cs^+-water island acquired at 5 K with a CO-terminated tip, which reveals that the Cs^+ and water molecules could form a periodic 1D array structure. The height profile analysis across the layer indicates that the cations display larger apparent heights than the water molecules due to the larger ion radius of Cs^+. Additionally, the height of the water region highlights the monolayer nature of the complex structure (Fig. 1a, lower-right panel). High-resolution STM image illustrates that the 2D Cs^+-water layer consists of single-stranded zigzag Cs^+ chains interconnected via water ring structures (Fig. 1a, lower-left panel). Although STM could resolve the position of Cs^+ cations, it is still challenging to identify the actual hydration shell and hydrogen(H)-bonding structure of the network.

To gain more details of the cation-water structure, a series of AFM investigations were conducted at varying tip heights (Fig. 1b and Supplementary Fig. 3)[34,40]. At a large tip height, the AFM image is

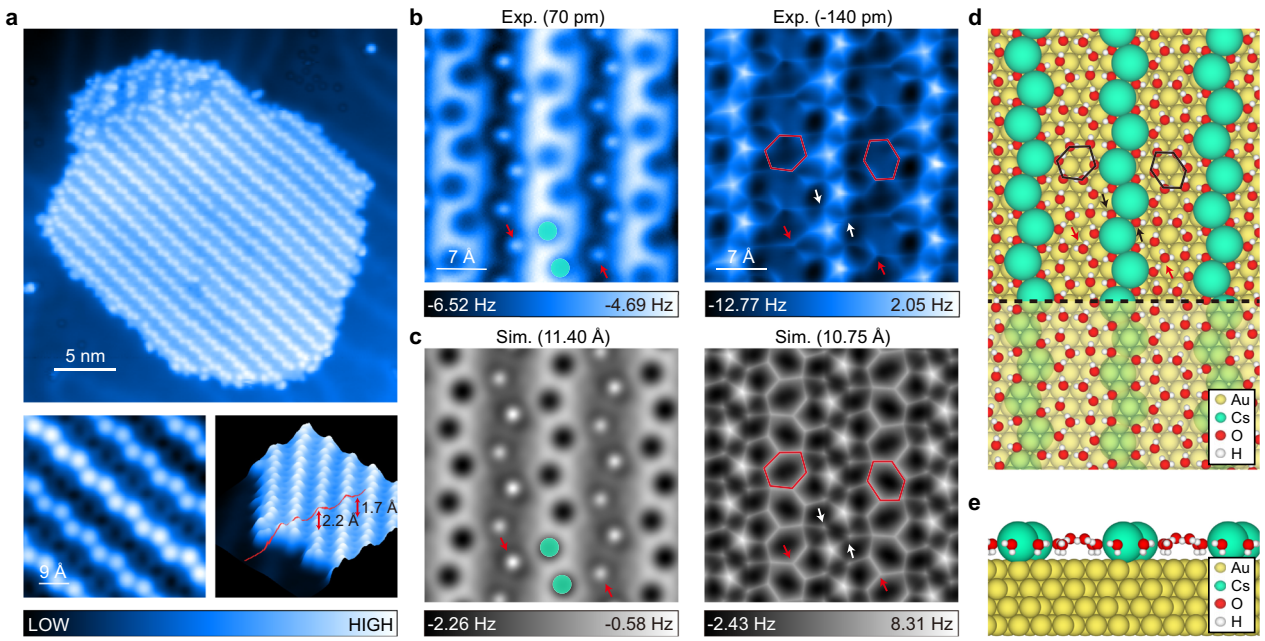

Fig. 1 | Atomic structure of Cs^+-water monolayer. a Constant-current STM images of 2D Cs^+-water layer on Au(111). Upper: The 2D Cs^+-water layer is composed of single-stranded zigzag Cs^+ chains. Lower left: The zoomed-in STM image of a 2D cation-water layer. Lower right: The line profile across the edge showing the heights of the layers, 1.7 (water molecules)–2.2 Å (Cs^+ cations). **b** Constant-height AFM (Δf) images at the tip heights of 70 pm (left) and −140 pm (right). **c** Simulated AFM images at the tip heights of 12.45 Å (left) and 11.00 Å (right). **d**, **e** Top (**d**) and side (**e**) views of the structural model of 2D Cs^+-water structure on the Au(111) surface. Au, Cs, H, and O atoms are denoted as yellow, cyan, white, and red spheres, respectively. The bridging water molecules are indicated by black (white) arrows in **d** (**b** and **c**). The flat-lying water molecules are indicated by red arrows in **b**–**d**. The water hexagons are indicated by black (red) dashed lines in **d** (**b** and **c**). The tip heights in **b** are referenced to the STM set point on the Au substrate (100 mV, 10 pA). The tip heights in **c** are defined as the vertical distance between the apex atom of the metal tip and the outmost atom of Au substrate. The oscillation amplitude of experimental and simulated images is 100 pm.

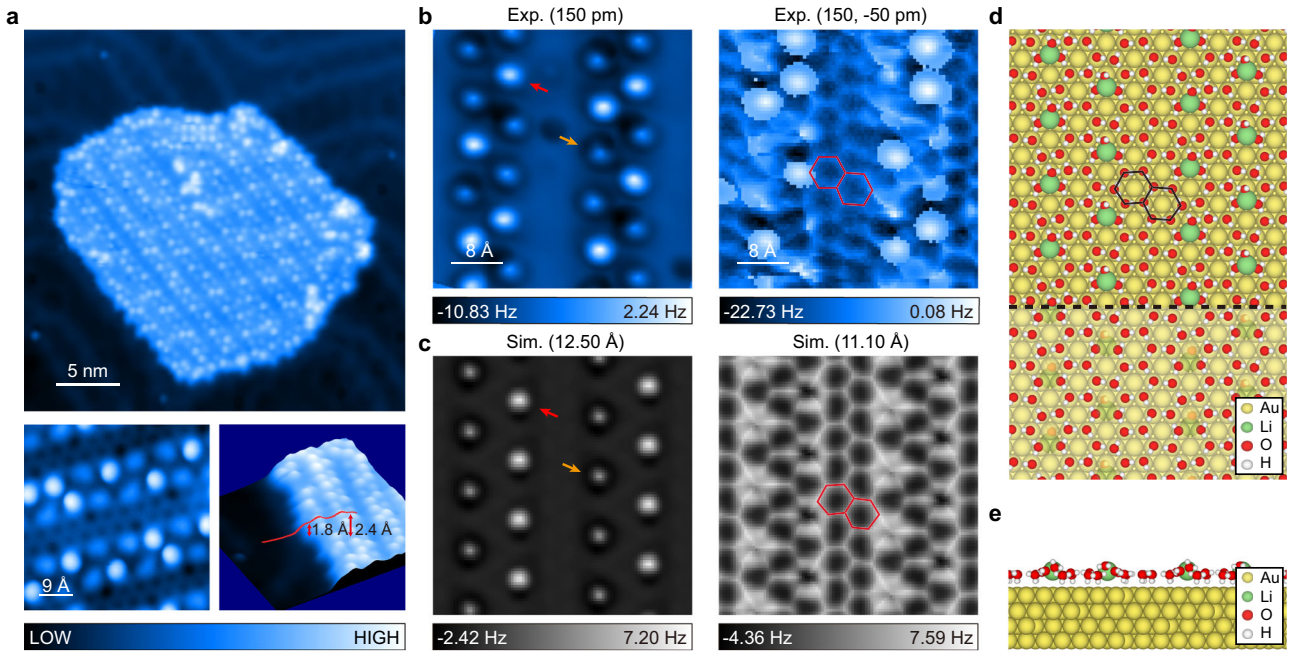

Fig. 2 | Atomic structure of Li^+-water monolayer. a Constant-current STM images of 2D Li^+-water layer on Au(111). Upper: The 2D Li^+-water layer is composed of double-stranded Li^+ chains. Lower left: The zoomed-in STM image of a 2D cation-water layer. Lower right: The line profile across the edge showing the heights of the layers, 1.8 (water molecules)−2.4 Å (water molecule on the top of Li^+ cation). **b** Constant-height AFM (Δf) image at 150 pm and varying-height AFM image with the original tip height of 150 pm, the threshold current of 7.6 pA and the height offset of −200 pm. **c** Simulated AFM images at the tip heights of 12.50 Å, and 11.10 Å. The brightness of the protrusions in AFM image at the large tip height is sensitive to the orientation of water molecule adsorbed on the top of Li^+. **d**, **e** Top (**d**) and side (**e**) views of the structural model of 2D Li^+-water structure on the Au(111) surface. Au, Li, H, and O atoms are denoted as yellow, green, white, and red spheres, respectively. The water hexagons are indicated by black (red) lines in **d** (**b** and **c**). The additional water molecules exhibit different orientations: H-up and flat, indicated by red and yellow arrows in **b** and **c**. The tip heights in **b** are referenced to the STM set point on the Au substrate (100 mV, 10 pA). The tip heights in **c** are defined as the vertical distance between the apex atom of the metal tip and the outmost atom of Au substrate. The oscillation amplitude of experimental and simulated images is 100 pm.

predominantly shaped by high-order electrostatic force, revealing a dark depression of the positively charged Cs^+, a consequence of its electrostatic attraction with the negatively charged CO-tip apex (Fig. 1b, left panel)[34]. Conversely, the water molecule was resolved as a bright feature, which is attributed to the negatively charged O atom (Supplementary Fig. 3). At a lower tip height, the Pauli repulsion force significantly influences the AFM signals, and the feature of cation turns to a bright protrusion (Fig. 1b, right panel). Moreover, the H bonds within the water molecules network were imaged as sharp-line features, resulting from the lateral relaxation of the CO-tip[41,42]. As shown in Fig. 1b, the AFM imaging could facilitate the discernment of the precise location of both cations and water molecules, indicating the alignment of Cs^+ ions in a zigzag pattern within a network of distorted hexagonal water rings.

Based on the insights from the high-resolution AFM images, a detailed atomic model for 2D Cs^+-water structure was proposed. This model, characterized by a 1:7 cation-water ratio, approximating 8 M concentration, was validated for structural stability using ab-initio DFT calculation (Fig. 1d). The theoretical AFM simulations indicated images in quantitative agreement with the experimental results (Fig. 1c, Supplementary Fig. 3 and Supplementary Table 1). Notably, each Cs^+ cation is hydrated by five water molecules, and two water molecules act as bridge between adjacent cations [indicated by white (black) arrows in Figs. 1b, c (d)]. The negatively charged surface preferentially orients most water molecules into an H-down configuration. But, some of the water molecules adopt a flat-lying configuration, critically influencing the formation of water hexagon structures between the neighbouring Cs^+ chains. Due to their weaker interaction with the surface, flat-lying water molecules are situated at a higher plane relative to the H-down ones, rendering them discernible as bright protrusions in the AFM images (Figs. 1b, c, left panel). Although the water molecules could form hexagonal water rings between the Cs^+ chains, the H-bonding network of water molecules exhibits high distortions, evidenced by variations in bond angles and the O-O distances ranging from 93° to 136° and 265 pm to 300 pm, respectively. (Supplementary Table 1)

Li^+-water monolayer with structured H-bonding network

To further explore the ion-specific effect on the water structure, we prepared a water overlayer on Au(111) surface mixed with Li^+ cations, which have much stronger interaction with water molecules than Cs^+ cation. The high-resolution STM image reveals that the 2D Li^+-water layer is composed of double-stranded Li^+ chains that are interconnected via a honeycomb water structure (Fig. 2a). The height and surface corrugation of the Li^+-water layer are more distinct than those observed in the Cs^+-water layer (Fig. 2a, lower-right panel). This pronounced height difference, together with the significantly smaller ion radius of Li^+ compared to Cs^+, suggest a 3D hydration structure of Li^+ cation. The AFM images provide further insight into the structure of the Li^+-water layer (Fig. 2b). At large and medium tip heights, AFM images reveal a bright protrusion (Fig. 2b) and a "Y"-shape feature at the Li^+ site (Supplementary Fig. 4), implying the presence of an addition water molecule adsorbed on the top of Li^+, causing a large height corrugation. The additional water molecules exhibit different orientations: H-up and flat, which could be distinguished by AFM images (indicated by red and yellow arrows respectively in Figs. 2b, c and Supplementary Fig. 4). The H-up configuration may become kinetically trapped during sample preparation (Supplementrary Text 2). It is worth noting that imaging the water molecules between the Li^+ chains proved challenging due to their much smaller height. We developed a varying-height AFM imaging technique and captured the information

of water molecules at different heights in the same image (Fig. 2b, right panel and Methods), showing that there is a hexagonal ice-like water structure between the Li^+ chains.

Based on our detailed AFM analysis, we propose an atomic structural model to describe the Li^+-water layer, characterized by a cation-water ratio of 1:12 (~ 5 M) (Fig. 2d). In this model, the water molecules form a hexagonal ice-like structure on the Au(111) surface, and the Li^+ cations adsorb at the bridge sites between two water molecules with a slight disturbance to the water network. An additional water monomer, exhibiting two orientations, is adsorbed on the top of Li^+, contributing to the large height corrugation shown in the STM/AFM images. Each Li^+ cation in this configuration is hydrated with three water molecules and elevated away from the surface (Supplementary Fig. 5). The model's accuracy is substantiated by the simulating AFM images (Fig. 2c, Supplementary Fig. 4 and Supplementary Table 2) that mirror our experimental results. Similar to the Cs^+-water layer, we note that the water molecules tend to adopt the H-down configuration, arising from the presence of negative charge distribution on the Au(111) surface (Supplementary Fig. 1).

Comparison of cation-water structure among Li^+, K^+ and Cs^+

We also investigated the 2D K^+-water layer with a cation-water ratio of approximately 1:6 (~ 9 M) on Au(111), whose properties fall in between Cs^+- and Li^+-water structures due to the interaction strength of K^+ with water molecules is stronger than Cs^+ and weaker than Li^+. The K^+ cations are hydrated with four water molecules and could form a compact chain through sharing water molecules like Cs^+ cations do (Supplementary Fig. 6). However, the K^+ and water could only assemble into short chains with random orientations, likely because the K^+-water and water-water interactions are comparable, resulting in the competitive structural arrangement. Meanwhile, the K^+ chains are interconnected by a honeycomb H-bonding network of water molecules, similar to the ice-like structure observed in the Li^+-water layer.

Based on the observations above, we can conclude three main features of cation-water layers along with the sequence of Li^+-K^+-Cs^+. Firstly, there is a sequential increase in the number of water molecules in the first hydration shell of each cation: three for Li^+, four for K^+, and five for Cs^+. Secondly, the cation-surface separation is decreased by removing the water layer between the cations and the surface, which indicates that the K^+ and Cs^+ cations would absorb the surface directly, potentially resulting in a site-blocking effect. Thirdly, the disturbance of cations on the H-bonding network of water increases. The Li^+ cation shows a structure-making effect, while the Cs^+ plays a structure-breaker role and the K^+ presents intermediate behavior. We also explore the double-layer alkali cation-water structures at diluted ion concentrations, which show similar properties to the single-layer structures (Supplementary Fig. 7). While our STM/AFM experiments were performed under high vacuum and low temperature, it is possible that those findings may have some relevance to the liquid/solid interface under ambient conditions considering the strong interaction between the cation-water layers and the charged surface[43,44]. Although the thermal fluctuations may suppress the lifetime of those structures, it is conceivable that certain intrinsic properties of ion-specific water structures could persist under ambient conditions. To support this, we employed in situ SEIRAS to probe interfacial water structure on the Au substrate immersed in alkaline (Fig. 3 and Supplementary Fig. 8), near neutral (Supplementary Fig. 9) and acidic (Supplementary Fig. 10) electrolytes containing different alkali metal cations.

Cation-dependent water structure at the electrolyte/electrode interface using in situ SEIRAS

In situ SEIRAS experiments were performed from the potential of zero charge (PZC) of polycrystalline Au (0.5 V_{RHE} at pH1 and 1.2 V_{RHE} at pH13) to HER relevant potential region (−0.3 V_{RHE} at pH1 and −0.6 V_{RHE} at pH13)[45–47], where the Au electrode surface is negatively charged. It should be noted that the PZC of Au does not change drastically with different facets (Supplementary Text 3). In addition, the negative surface charge density of Au(111) surface at the conditions of STM/AFM measurements was −0.15 (Li^+-water layer)~−0.20 (Cs^+-water layer) As m^{-2} as suggested by ab initio DFT calculations. Thus, the surface potential of Au(111) surface at STM/AFM conditions can be estimated at −0.45 V versus PZC for Li^+ and −0.3 V versus PZC for Cs^+ by using the Gouy-Chapman-Stern model (Supplementary Fig. 11 and Supplementary Text 4), which correlate with pre-HER relevant potential in SEIRAS and electrochemical measurements.

To investigate the impact of alkali cations on the interfacial water structure, we examined the OH stretching modes (~ 3600-3200 cm^{-1}) of water molecules at the Au/electrolyte interface. Figure 3a–c displays the SEIRAS spectra of OH stretching at pH13 in aqueous electrolytes of 0.1 M hydroxide of Li^+, K^+ and Cs^+. At potentials below PZC, the Au surface was negatively charged. Moving to low electrode potentials could increase the negative surface charge, which could enhance the interaction between the water dipole and the electrified interface. Consequently, the intensity of OH stretching peak increases as the potential decreases from 1 to −0.6 V_{RHE}.

We further deconvoluted the OH stretching band by three peaks at 3600, 3450, and 3240 cm^{-1}, representing weakly H-bonded (isolated) water molecules, asymmetrically H-bonded water molecules within the hydration shell, and symmetrically H-bonded ice-like water molecules on Au, respectively, as shown in Fig. 3d for −0.6 V_{RHE} (Supplementary Fig. 12 for other potentials)[24]. The potential-dependent relative fractions of deconvoluted peaks for isolated water, asymmetrically and symmetrically H-bonded water molecules are shown in Figs. 3e–g. By comparing the relative fractions of different peaks for different cations, we found that the Cs^+ promotes weakly H-bonded (isolated) water molecules at negatively charged Au/electrolyte interface, whereas the Li^+ predominantly promotes symmetric H-bonded ones, which suggests that the Li^+ reinforces the H-bonding network of interfacial water, rendering it more structured than that of Cs^+ and K^+. These observations qualitatively agree with the results obtained from AFM/STM experiments (Figs. 1, 2 and Supplementary Fig. 6). Similar cation-dependent interfacial water features were observed at pH6-7 and pH1 (Supplementary Figs. 9, 10).

Cation- and pH-dependent HER kinetics

In order to further explore the effect of alkali cations on the actual electrochemical reaction, we evaluated HER experiments at different pH values and analyzed the reaction kinetics to obtain insights into the microscopic mechanism. The cation- and pH-dependent HER polarization curves on Au rotating disk electrode (RDE) are shown in Figs. 4a–c (Supplementary Fig. 13). The HER exchange current density decreases in the order of $Li^+ > Na^+ > K^+ > Cs^+$ in acidic, neutral and alkaline electrolytes (Fig. 4d). The cation-dependence of HER kinetics on polycrystalline Au surface can be attributed to the accumulation of cations at electrified interface, namely weakly hydrated cations (K^+ and Cs^+) show higher near-surface concentration in comparison to a strongly hydrated cation (Li^+), which is also evidenced in our STM/AFM results. The higher near-surface concentration of weakly hydrated cations could inhibit HER kinetics on Au surface by blocking the active sites[44] and altering the interfacial hydrogen bonding network[13]. Furthermore, consistent with the observation by Monteiro et al.[44], we found that weakly hydrated cations (K^+ and Cs^+) favour HER on gold only at low overpotentials compared to strongly hydrated cations (Li^+) (Supplementary Fig. 13c), whereas at high overpotentials a lower HER activity has been observed in the electrolytes containing weakly hydrated cations (K^+ and Cs^+) (Fig. 4c). The promotion (at lower overpotentials) and inhibition (at higher overpotentials) of HER on Au

https://doi.org/10.1038/s41467-024-52131-w

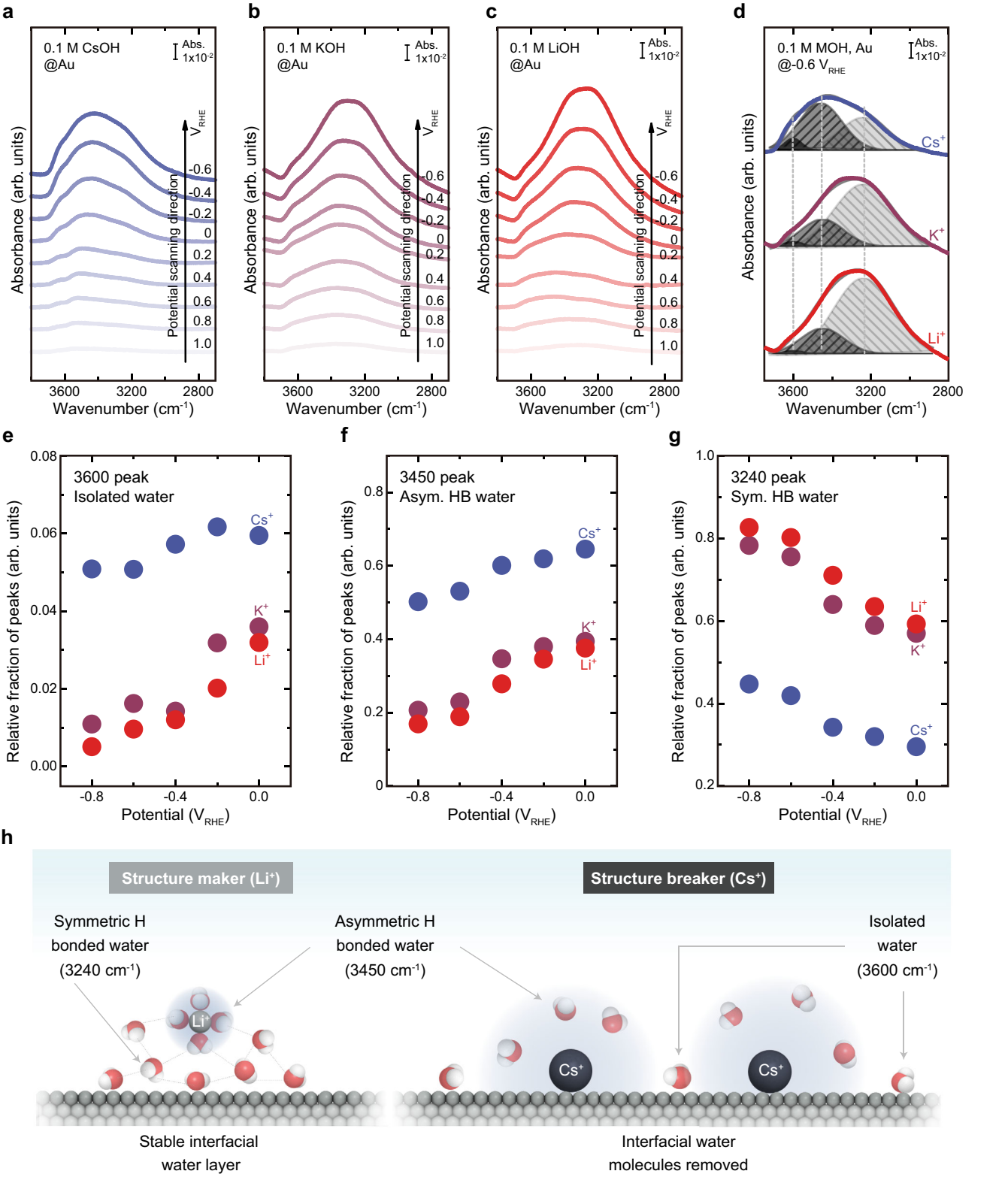

Fig. 3 | Altering interfacial structure at Au surface in aqueous electrolytes. **a**–**c** The potential-dependent OH stretching features of in situ SEIRAS spectra at pH13 in a H_2-saturated aqueous solution of 0.1 M of LiOH, KOH, and CsOH, respectively, where the reference spectrum was taken at 1.1 V_{RHE}. Full spectra before and after subtracting by reference spectrum (at 1.1 V_{RHE}) are available in Supplementary Fig. 8. **d** The deconvolution of the OH stretching peak of spectra acquired at −0.6 V_{RHE}, where OH stretching peak was deconvoluted into three components: 1) 3600 cm^{-1} with width=160 cm^{-1} (isolated water), 2) 3450 cm^{-1} with width=260 cm^{-1} (asymmetrically H-bonded water), and 3) 3240 cm^{-1} with width=250 cm^{-1} (symmetrically H-bonded water). The deconvolution of OH stretching peak at other potentials is shown in Supplementary Fig. 12. **e**–**g** The potential- and cation-dependence of the relative fraction of peaks at 3600 cm^{-1}, 3450 cm^{-1}, and 3240 cm^{-1}. **h** A schematic showing that Li^+ promotes symmetric H-bonded water at the interface while Cs^+ tends to form isolated water molecules at the Au surface.

https://doi.org/10.1038/s41467-024-52131-w

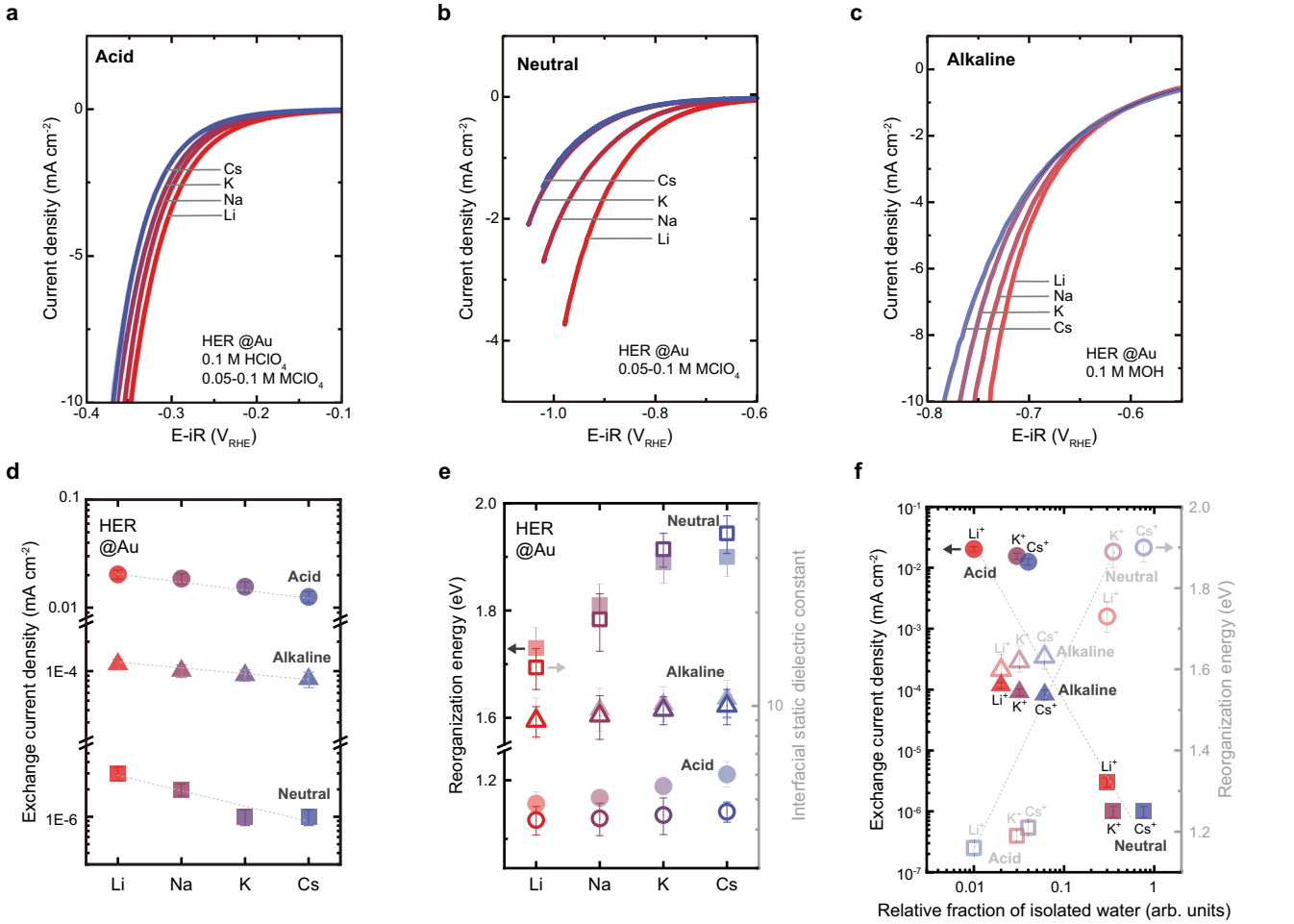

Fig. 4 | Cation-dependent and pH-dependent HER kinetics on Au RDE electrode. a–c HER polarization curves on Au surface in acidic, neutral and alkaline electrolytes, respectively, measured at 10 mV s^{-1} and 2500 rpm in H_2-saturated aqueous electrolytes of 0.1 M $HClO_4$ and 0.1 M perchlorate salt of Li, Na, K or 0.05 M perchlorate salt of Cs (pH1), aqueous solutions of 0.05–0.1 M $MClO_4$ (M=Li, Na, K and Cs) (pH6-7), and aqueous electrolytes of 0.1 M hydroxide of Li, Na, K and Cs (pH13). The zoom-in of low overpotential region can be found in Supplementary Fig. 13. **d** The exchange current density extracted by MHC formalism (Supplementary Fig. 15). **e** The reorganization energy extracted by MHC formalism and interfacial static dielectric constant extracted via Born model of reorganization energy. **f** The reorganization energy of HER on Au RDE as a function of the relative fraction of isolated water in OH stretching peak at −0.2 V_{RHE} for acidic, neutral and alkaline electrolytes. All CV data has been iR corrected. The non-iR corrected HER polarization curves are shown in Supplementary Fig. 16. Error bars were obtained from the standard deviation of 2–3 independent measurements.

surfaces has been attributed to cation concentration effect on Volmer step. Due to the low solubility of perchlorate salt of Cs^+, we employed 0.1 M chloride salts of Li^+, K^+ and Cs^+ to confirm the cation-dependence of HER kinetics on Au in 0.1 M $HClO_4$ at pH1 (Supplementary Fig. 14), observing a similar cation trend but with a more pronounced effect for chloride salts compared to perchlorate salts. On the other hand, HER kinetics on polycrystalline Au was shown to be pH dependent. Specifically, the HER kinetics in acidic electrolytes (pH1) exhibited a higher j_0 than that in alkaline electrolytes (pH13). The pH dependence of HER kinetics on Au is similar to the trend of HER/HOR kinetics on Pt group metal surfaces in previous studies[48–50], which can be attributed to the pH-dependent interfacial water structure rather than pH-dependent hydrogen-binding energy (HBE)[12,13,51]. The HER kinetics in 0.05 M perchlorate salt at near-neutral condition (pH6-7) showed the lowest j_0 among all the three pH, due to proton transport limitation at near-neutral pH[52].

Discussion

Based on our investigations, we further established a correlation between HER kinetics and the solvation environment at the electrified interface. Employing Marcus-Hush-Chidsey (MHC) formalism and Born model, we revealed that the HER exchange current density decreased, while the reorganization energy and the interfacial dielectric constant increased with an increasing trend of alkali metal cation from Li^+ to Cs^+ (Figs. 4d–f, Supplementary Fig. 15 and Supplementary Text 5). Our SEIRAS and STM/AFM experiments (Figs. 1–3 and Supplementary Figs. 8 to 10) converge on the finding that structure-breaking cations (such as Cs^+) could interact strongly with negatively charged Au surface, consequently, displace interfacial water molecules and suppress the interfacial H-bonding network, leading to isolated or weakly H-bonded water molecules on the Au surface. Conversely, structure-making cations (such as Li^+) could retain their solvation structure and migrate from the substrate through water molecules, promoting a more structured interfacial water layer with a more abundant ice-like H-bonding network. These results potentially offer atomic-level insight into the kinetic properties. The structured H-bonding network at the interface demonstrates enhanced structural stability, exhibits diminished responsiveness to the change of electrode potential, and consequently, shows a lower interfacial dielectric constant (Fig. 4e). The interfacial solvation environment exhibits a weakly H-bonded network with distorted H-bonding angles and varied bonding lengths. These irregularities yield a larger interfacial dielectric

constant and increased reorganization energy, which impedes proton transfer during electrochemical reactions and leads to an increase in the PECT barrier in the Volmer and the Heyrovsky steps in HER kinetics. In contrast, the strongly H-bonded interface could facilitate PCET processes on Pt[13] and Au (this work) surfaces.

We carefully fabricated and systematically characterized the 2D network of water molecules and alkali metal cations (Li^+, K^+ and Cs^+) on a charged Au(111) surface. The STM/AFM results contribute real-space insights into the ion-specific water structures on metal surfaces, which are qualitatively aligned with the SEIRAS experiments of electrolyte/electrode interfaces under ambient conditions. These results not only provide a further understanding of the atomic structure at liquid/solid interfaces but also reveal the important role of ions in the electrochemical reactions at the atomic scale. We expect that our methods can be further applied to a large variety of cations and anions, to construct different model systems for studying various ion-water structures at different electrode surfaces. Recently, the atomic structures of the bulk insulating ice Ih surface have been observed using qPlus AFM technique[53]. Additionally, by integrating nanosecond laser transient heating and rapidly re-freezing technology[54] into the AFM system, it is possible to capture the liquid-like states and the dynamics of water and ions. These technological advancements could present an opportunity for future exploration into ion-specific water multilayer structures.

Methods

STM/AFM experiments

All the STM and non-contact AFM experiments were performed using Createc (Germany) and CASAcme (China) instruments. These investigations were conducted at a cryogenic temperature of 5 K, utilizing a custom-made qPlus sensor equipped with a tungsten (W) tip, featuring a spring constant (k0) of approximately 1800 $N{\cdot}m^{-1}$, a resonance frequency (f_0) of around 28.7 kHz, and a high-quality factor (Q) in the order of 100,000. The bias voltage is defined relative to the potential difference between the sample and the probe tip. The CO-terminated tips were employed to acquire both STM topographic images and AFM frequency shift (Δf) images, using constant-current and constant-height modes, respectively, except for those specified in the text. The process for creating a CO-terminated tip involves precisely aligning the metallic tip above a CO molecule residing on the Au(111) surface—initially set at a voltage of 100 mV and current of 10 pA—and incrementally increasing the tunnelling current to 400 pA to facilitate the tip's termination.

In order to verify the precise 3D structure of Li^+-water layer, we used a varying-height AFM method, in which the tip was approached to the surface by a height offset as long as the detected current value was smaller than the set threshold value, so that the H-bonding skeleton of lower water molecules surrounding the higher water molecules could be clearly resolved.

Sample preparation

The Au(111) single crystal employed in this studies was purchased from MaTeck and underwent a cleaning process, fllowing repeated Ar^+ ion sputtering at 1 keV and annealing at about 700 K for multiple cycles. The SAES alkali-metal dispensers were used to deposite alkali metal atoms. The dispensers were degassed, with regulated currents set for the evaporation of lithium (I_{Li} = 8.5 A), potassium (I_K = 6.5 A), and cesium (I_{Cs} = 5.5 A) over a duration of 2 min. The alkali metal atoms were deposited on the Au(111) surface at room temperature, with deposition current I_{Li} = 8.3 A, I_K = 6.3 A, I_{Cs} = 5.2 A, duration of 1 min. The ultrapure H_2O was purchased from Sigma Aldrich, with a maximum deuterium content limited to 1 ppm. The water was subjected to additional purification under vacuum by 3–5 freeze-and-pump cycles to remove remaining gas impurities.

DFT calculations

DFT calculations were conducted employing the Vienna ab initio simulation package (VASP)[55,56]. The calculations used projector augmented wave pseudopotentials with a cut-off energy of 550 eV for the description of the electronic wave functions[57]. To address the van der Waals interactions for dispersion forces, were considered by using the optB86b-vdW exchange-correlation functional was employed[58,59]. In modeling the Au(111) surface, a slab comprising four layers was constructed, with all but the topmost layer fixed to emulate the bulk-like properties of the substrate. The gold lattice constant was set to be 4.073 Å. For Li^+ system, a $(2\sqrt{3}\times\sqrt{57})$ supercell and a $(2\times1\times1)$ Monkhorst–Pack (MP) grid were used for the Brillouin zone sampling. For K^+ system, a $(5\times\sqrt{3})$ supercell and a $(2\times7\times1)$ MP grid were implemented. For Cs^+ system, a $(\sqrt{97}\times2\sqrt{3})$ supercell and a $(1\times3\times1)$) MP grid were applied. A vacuum layer thickness exceeding 16 Å was instituted to preclude spurious interactions between periodic images, with dipole corrections being applied along the surface normal direction[60,61]. The procedure of geometry optimization was performed with a force criterion of 0.01 $eV\cdot Å^{-1}$. To provide an incisive assessment of charge distribution on the optimized geometries, Bader charge analysis was performed[62].

AFM Simulations

To simulate the frequency shift (Δf) images, a molecular mechanics model encapsulating electrostatic forces was used, based on the methods described in ref. 63. The flexible probe-particle tip model was used. This model assigns an effective lateral stiffness k = 0.75 $N{\cdot}m^{-1}$ and defines the effective atomic radius R_c = 1.661 Å. To mimic the characteristics of a CO-terminated tip, a quadrupole-like (d_{z^2}) charge distribution was prescribed at the tip apex, with an inherent charge q = −0.1 e. Electrostatic potentials from DFT calculations were employed in AFM simulations. The Lennard-Jones potential parameters for element interactions are detailed Supplementary Table 3. The tip height is defined as the vertical distance from the tip apex to the substrate's top atomic layer. The oscillation amplitude of the simulated AFM images was 100 pm.

Electrochemical measurements and electrolyte preparation

For all electrochemical measurements, a three-electrode electrochemical system and a Biologic SP-300 potentiostat were employed[13]. A polycrystalline Au rotating disk electrode (RDE) (E3PK series fixed-disk, Pine instrument) was used as the working electrode. Before each measurement, the electrode surface was polished with successively finer-grade diamond slurries down to 0.25 μm. A gold foil (thickness 0.1 mm, Sigma-Aldrich 99.99%) was used counter electrodes. Potentials were recorded versus a mercury sulfate ($Hg/HgSO_4$) reference electrode in acidic and neutral solutions and to a mercury oxide (Hg/HgO) reference electrode in alkaline electrolytes. The mercury sulfate ($Hg/HgSO_4$) reference electrode was calibrated in H_2-saturated 0.1 M $HClO_4$ elelctrolyte using a polycristalline Pt RDE, with a potential value of 0.355 V_{SHE}. The mercury oxide (Hg/HgO) reference electrode was calibrated in H_2-saturated 0.1 M KOH elelctrolyte using a polycristalline Pt RDE, with a potential value of 0.867 V_{SHE}. All potentials were converted to the RHE scale using $E_{RHE} = E_{meas} + E_{RE} + 0.059\times pH$. A standard glass electrochemical cell with a water jacket (150 mL, Pine research instrument) was used for the measurements in acidic and neutral electrolytes. For experiemnts in alkaline electrolytes, an alkaline-resistant PTFE cell (175 mL, Pine research instrument) was utilized.

The effects of pH and cations on the kinetics of HER were examined by CV measurements at a scan rate of 10 mV s^{-1} at 2500 rpm in H_2 saturated solutions at 293 K. The normalized current density was obtained using the geometric surface area of RDE (0.196 cm^2) and the reported potentials were iR corrected. The ohmic resistance value of each experiment was summarized in Supplementary Table 7. The pH of

the electrolytes was measured using a digital desktop laboratory pH-meter (PHS-3C, Puchun). The pH values of all electrolytes were summarized in Supplementary Table 8. Neutral solutions, acidic and alkaline electrolytes were prepared from deionized water (Millipore, >18.2 MΩ.cm). For cation-dependent measurements, 0.05–0.1 M perchlorate salt of Li^+, Na^+, K^+ and Cs^+ ($LiClO_4$, Sigma-Aldrich 99.99%; $NaClO_4$, Sigma-Aldrich 99.9%; $KClO_4$, Sigma-Aldrich 99.99%; $CsClO_4$, Sigma-Aldrich 99.9%) were added to 0.1 M $HClO_4$ (Sigma-Aldrich 70 wt% and 99.999% trace metal basis) at pH1. 0.05–0.1 M perchlorate salts of Li^+, Na^+, K^+ and Cs^+ ($LiClO_4$, Sigma-Aldrich 99.99%; $NaClO_4$, Sigma-Aldrich 99.9%; $KClO_4$, Sigma-Aldrich 99.99%; $CsClO_4$, Sigma-Aldrich 99.9%) were used to prepare electrolytes at neutral pH. Alkaline electrolytes at pH13 were prepared with aqueous solutions of 0.1 M hydroxides of Li^+, Na^+, K^+ and Cs^+ (LiOH, Sigma-Aldrich 99.99%; NaOH, Sigma-Aldrich 99.9%; KOH, Sigma-Aldrich 99.95%; CsOH, Sigma-Aldrich 99.95%). The electrolyes were prepared and stored at ambient conditions, and were used for experiements within 1–2 h of preparation.

In situ Surface-Enhanced Infrared Absorption Spectroscopy (SEIRAS)

The reflecting plane of the hemispherical Si prism (radius 22 mm, Pier optics) on which gold thin film is deposited was polished with successively finer grade diamond slurries down to 0.25 µm. Then the surface was contacted with 40% NH_4F for 90 s to remove oxide layer on the Si surface and to terminate it with hydrogen. Deposition of Au was performed at 60 °C simply by dropping a mixture of a plating solution and 2% HF (1:1 in volume) onto the hydrogen-terminated Si surface. The composition of the plating solution was 0.0075 M $NaAuCl_2$, 0.075 M Na_2SO_3, 0.025 M Na_2SO_3 and 0.025 M NH_4Cl. At 60–90 s after dropping the plating solution, the prism was rinsed with Milli-Q water to finish the deposition.

The Au-deposited hemispherical Si prism was mounted in a spectro-electrochemical three-electrode system (Supplementary Fig. 17). A mercury oxide electrode (Hg/HgO) and a gold foil (thickness 0.1 mm, Sigma-Aldrich 99.99%) were used as the reference and counter electrodes. Prior to measurements, the Au surface was cleaned electrochemically in 0.1 M $HClO_4$ by repeating potential scans between 0 and 1.3 V_{RHE}. The SEIRAS measurements were performed using a Bruker Vertex 70 Fourier-Transform Infrared (FTIR) spectrometer, equipped with a MCT detector. The optical path was fully replaced with N_2 gas. The SEIRAS spectra were recorded with a resolution of 4 cm^{-1} at a scan velocity of 7.5 kHz covering the 500–4000 cm^{-1} spectral range; with an average of 64 scans. A single reflection ATR (Attenuated Total Reflection) accessory (Pike Vee-Max II, Pike Technologies) with a Au deposited Si prism at an incident angle of 68° was used. The enhanced region was estimated to be around 10 nm of the surface[64] (Supplementary Text 6). For in situ SEIRAS measurements during HER in electrolytes at pH1 in 0.1 M $HClO_4$ (Sigma-Aldrich 70 wt% and 99.999% trace metal basis) and 0.05–0.1 M perchlorate salt of Li^+, K^+ and Cs^+ ($LiClO_4$, Sigma-Aldrich 99.99%; $NaClO_4$, Sigma-Aldrich 99.9%; $KClO_4$, Sigma-Aldrich 99.99%; $CsClO_4$, Sigma-Aldrich 99.9%); at neutral pH in 0.05 M perchlorate salt of Li^+, K^+ and Cs^+ ($LiClO_4$, Sigma-Aldrich 99.99%; $NaClO_4$, Sigma-Aldrich 99.9%; $KClO_4$, Sigma-Aldrich 99.99%; $CsClO_4$, Sigma-Aldrich 99.9%); at pH13 in 0.1 M of hydroxide of Li^+, K^+ and Cs^+ (LiOH, Sigma-Aldrich 99.99%; NaOH, Sigma-Aldrich 99.9%; KOH, Sigma-Aldrich 99.99%; CsOH, Sigma-Aldrich 99.9%) were saturated with H_2 by purging H_2 gas. Before conducting in situ SEIRAS experiments, the Au-deposited Si prism surface was cleaned by cycling the potential between 0.05 and 1.1 V_{RHE}. SEIRAS spectra were then collected at potentials ranging from 1.1 V_{RHE} to HER relevant potential region. The reference spectrum, I_0, was recorded at 1.1 V_{RHE}. All spectra are presented in absorbance units, defined as $\log(I_0/I)$, where I_0 and I correspond to the reference and sample spectra, respectively. The same Au surface was used for measurements at a given pH to ensure similar surface enhancement effects.

Data availability

The tabulated data used to create the figures have been deposited at Zenodo (https://doi.org/10.5281/zenodo.13634826)[65]. All data needed to evaluate the conclusions in the paper are present in the paper or the Supplementary Information. Source data are provided in this paper.

References

1. Devanathan, M. A. & Tilak, B. V. K. Structure of electrical double layer at metal-solution interface. *Chem. Rev.* **65**, 635–684 (1965).
2. Stamenkovic, V. R., Strmcnik, D., Lopes, P. P. & Markovic, N. M. Energy and fuels from electrochemical interfaces. *Nat. Mater.* **16**, 57–69 (2017).
3. Simon, P. & Gogotsi, Y. Materials for electrochemical capacitors. *Nat. Mater.* **7**, 845–854 (2008).
4. Subbaraman, R. et al. Enhancing hydrogen evolution activity in water splitting by tailoring Li^+-$Ni(OH)_2$-Pt interfaces. *Science* **334**, 1256–1260 (2011).
5. Choi, N. S. et al. Challenges facing lithium batteries and electrical double-layer capacitors. *Angew. Chem. Int. Ed.* **51**, 9994–10024 (2012).
6. Stern, O. ZUR THEORIE DER ELEKTROLYTISCHEN DOPPELSCHICHT. *Zeitschrift für Elektrochemie und angewandte physikalische Chemie* **30**, 508–516 (1924).
7. Strmcnik, D. et al. The role of non-covalent interactions in electrocatalytic fuel-cell reactions on platinum. *Nat. Chem.* **1**, 466–472 (2009).
8. Liu, M. et al. Enhanced electrocatalytic CO_2 reduction via field-induced reagent concentration. *Nature* **537**, 382–386 (2016).
9. Resasco, J. et al. Promoter effects of alkali metal cations on the electrochemical reduction of carbon dioxide. *J. Am. Chem. Soc.* **139**, 11277–11287 (2017).
10. Ringe, S. et al. Double layer charging driven carbon dioxide adsorption limits the rate of electrochemical carbon dioxide reduction on Gold. *Nat. Commun.* **11**, 1–11 (2020).
11. Gu, J. et al. Modulating electric field distribution by alkali cations for CO_2 electroreduction in strongly acidic medium. *Nat. Catal.* **5**, 268–276 (2022).
12. Ledezma-Yanez, I. et al. Interfacial water reorganization as a pH-dependent descriptor of the hydrogen evolution rate on platinum electrodes. *Nat. Energy* **2**, 1–7 (2017).
13. Huang, B. et al. Cation- and pH-dependent hydrogen evolution and oxidation reaction kinetics. *JACS Au* **1**, 1674–1687 (2021).
14. Monteiro, M. C. O. et al. Absence of CO_2 electroreduction on copper, gold and silver electrodes without metal cations in solution. *Nat. Catal.* **4**, 654–662 (2021).
15. Shah, A. H. et al. The role of alkali metal cations and platinum-surface hydroxyl in the alkaline hydrogen evolution reaction. *Nat. Catal.* **5**, 923–933 (2022).
16. Ovalle, V. J., Hsu, Y. S., Agrawal, N., Janik, M. J. & Waegele, M. M. Correlating hydration free energy and specific adsorption of alkali metal cations during CO_2 electroreduction on Au. *Nat. Catal.* **5**, 624–632 (2022).
17. Grosberg, A. Y., Nguyen, T. T. & Shklovskii, B. I. Colloquium: The physics of charge inversion in chemical and biological systems. *Rev. Mod. Phys.* **74**, 329–345 (2002).
18. Lyklema, J. Quest for ion-ion correlations in electric double layers and overcharging phenomena. *Adv. Colloid Interface Sci.* **147-48**, 205–213 (2009).
19. Toney, M. F. et al. Voltage-dependent ordering of water-molecules at an electrode-electrolyte interface. *Nature* **368**, 444–446 (1994).

20. Velasco-Velez, J. J. et al. The structure of interfacial water on gold electrodes studied by x-ray absorption spectroscopy. *Science* **346**, 831–834 (2014).
21. Intikhab, S., Snyder, J. D. & Tang, M. H. Adsorbed hydroxide does not participate in the volmer step of alkaline hydrogen electrocatalysis. *ACS Catal.* **7**, 8314–8319 (2017).
22. Hao, Y. C. et al. Promoting nitrogen electroreduction to ammonia with bismuth nanocrystals and potassium cations in water. *Nat. Catal.* **2**, 448–456 (2019).
23. Zou, S. Z., Chen, Y. X., Mao, B. W., Ren, B. & Tian, Z. Q. SERS studies on electrode/electrolyte interfacial water .1. Ion effects in the negative potential region. *J. Electroanal. Chem.* **424**, 19–24 (1997).
24. Ataka, K., Yotsuyanagi, T. & Osawa, M. Potential-dependent reorientation of water molecules at an electrode/electrolyte interface studied by surface-enhanced infrared absorption spectroscopy. *J. Phys. Chem.* **100**, 10664–10672 (1996).
25. Nihonyanagi, S. et al. Potential-dependent structure of the interfacial water on the gold electrode. *Surf. Sci.* **573**, 11–16 (2004).
26. Li, C. Y. et al. In situ probing electrified interfacial water structures at atomically flat surfaces. *Nat. Mater.* **18**, 697–701 (2019).
27. Dunwell, M., Wang, J. H., Yan, Y. & Xu, B. Surface enhanced spectroscopic investigations of adsorption of cations on electrochemical interfaces. *Phys. Chem. Chem. Phys.* **19**, 971–975 (2017).
28. Liu, Y. H., Kawaguchi, T., Pierce, M. S., Komanicky, V. & You, H. Layering and ordering in electrochemical double layers. *J. Phys. Chem. Lett.* **9**, 1265–1271 (2018).
29. Nakamura, M., Nakajima, Y., Sato, N., Hoshi, N. & Sakata, O. Structure of the electrical double layer on Ag(100): Promotive effect of cationic species on Br adlayer formation. *Phys. Rev. B* **84**, 165433 (2011).
30. Wang, Y. H. et al. In situ Raman spectroscopy reveals the structure and dissociation of interfacial water. *Nature* **600**, 81–85 (2021).
31. Garcia-Araez, N., Rodriguez, P., Navarro, V., Bakker, H. J. & Koper, M. T. M. Structural effects on water adsorption on gold electrodes. *J. Phys. Chem. C* **115**, 21249–21257 (2011).
32. Li, P. et al. Hydrogen bond network connectivity in the electric double layer dominates the kinetic pH effect in hydrogen electrocatalysis on Pt. *Nat. Catal.* **5**, 900–911 (2022).
33. Giessibl, F. J. The qPlus sensor, a powerful core for the atomic force microscope. *Rev. Sci. Instrum.* **90**, 011101 (2019).
34. Peng, J. B. et al. The effect of hydration number on the interfacial transport of sodium ions. *Nature* **563**, 701–705 (2018).
35. Tian, Y. et al. Visualizing Eigen/Zundel cations and their interconversion in monolayer water on metal surfaces. *Science* **377**, 315–319 (2022).
36. Tian, Y. et al. Nanoscale one-dimensional close packing of interfacial alkali ions driven by water-mediated attraction. *Nat. Nanotechnol.* **19**, 479–485 (2024).
37. Garlyyev, B., Xue, S., Watzele, S., Scieszka, D. & Bandarenka, A. S. Influence of the nature of the alkali metal cations on the electrical double-layer capacitance of model Pt(111) and Au(111) electrodes. *J. Phys. Chem. Lett.* **9**, 1927–1930 (2018).
38. Brown, M. A., Goel, A. & Abbas, Z. Effect of electrolyte concentration on the Stern layer thickness at a charged interface. *Angew. Chem. Int. Ed.* **55**, 3790–3794 (2016).
39. Cheng, J. & Sprik, M. The electric double layer at a rutile TiO_2 water interface modelled using density functional theory based molecular dynamics simulation. *J. Phys.: Condens. Matter* **26**, 244108 (2014).
40. Gross, L., Mohn, F., Moll, N., Liljeroth, P. & Meyer, G. The chemical structure of a molecule resolved by atomic force microscopy. *Science* **325**, 1110–1114 (2009).
41. Shiotari, A. & Sugimoto, Y. Ultrahigh-resolution imaging of water networks by atomic force microscopy. *Nat. Commun.* **8**, 1–7 (2017).
42. Ma, R. Z. et al. Atomic imaging of the edge structure and growth of a two-dimensional hexagonal ice. *Nature* **577**, 60–63 (2020).
43. Goyal, A. & Koper, M. T. M. The interrelated effect of cations and electrolyte pH on the hydrogen evolution reaction on gold electrodes in alkaline media. *Angew. Chem. Int. Ed.* **60**, 13452–13462 (2021).
44. Monteiro, M. C. O., Goyal, A., Moerland, P. & Koper, M. T. M. Understanding cation trends for hydrogen evolution on platinum and gold electrodes in alkaline media. *ACS Catal.* **11**, 14328–14335 (2021).
45. Kolb, D. M. & Schneider, J. Surface reconstruction in electrochemistry - Au(100)-(5x20), Au(111)-(1x23) and Au(110)-(1x2). *Electrochim. Acta* **31**, 929–936 (1986).
46. Bode, D. D., Andersen, T. N. & Eyring, H. Anion and pH effects on the potentials of zero charge of gold and silver electrodes. *J. Phys. Chem.* **71**, 792–797 (1967).
47. Bodé, D. D., Andersen, T. N. & Eyring, H. Cation effects on the potentials of zero charge of gold, silver, and mercury electrodes. *J. Electrochem. Soc.* **114**, 72 (1967).
48. Durst, J. et al. New insights into the electrochemical hydrogen oxidation and evolution reaction mechanism. *Energy Environ. Sci.* **7**, 2255–2260 (2014).
49. Sheng, W. C., Gasteiger, H. A. & Shao-Horn, Y. Hydrogen oxidation and evolution reaction kinetics on platinum: Acid vs alkaline electrolytes. *J. Electrochem. Soc.* **157**, B1529–B1536 (2010).
50. Ringe, S. Cation effects on electrocatalytic reduction processes at the example of the hydrogen evolution reaction. *Curr. Opin. Electrochem.* **39**, 101268 (2023).
51. Rebollar, L. et al. "Beyond adsorption" descriptors in hydrogen electrocatalysis. *ACS Catal.* **10**, 14747–14762 (2020).
52. Strmcnik, D., Lopes, P. P., Genorio, B., Stamenkovic, V. R. & Markovic, N. M. Design principles for hydrogen evolution reaction catalyst materials. *Nano Energy* **29**, 29–36 (2016).
53. Hong, J. et al. Imaging surface structure and premelting of ice Ih with atomic resolution. *Nature***630**,375–380 (2024).
54. Kringle, L., Thornley, W. A., Kay, B. D. & Kimmel, G. A. Reversible structural transformations in supercooled liquid water from 135 to 245 K. *Science* **369**, 1490–1492 (2020).
55. Kresse, G. Ab-initio molecular-dynamics for liquid-metals. *J. Non-Cryst. Solids* **193**, 222–229 (1995).
56. Kresse, G. & Furthmuller, J. Efficient iterative schemes for ab initio total-energy calculations using a plane-wave basis set. *Phys. Rev. B* **54**, 11169–11186 (1996).
57. Kresse, G. & Joubert, D. From ultrasoft pseudopotentials to the projector augmented-wave method. *Phys. Rev. B* **59**, 1758–1775 (1999).
58. Klimes, J., Bowler, D. R. & Michaelides, A. Chemical accuracy for the van der Waals density functional. *J. Phys.: Condens. Matter* **22**, 022201 (2010).
59. Klimes, J., Bowler, D. R. & Michaelides, A. Van der Waals density functionals applied to solids. *Phys. Rev. B* **83**, 195131 (2011).
60. Neugebauer, J. & Scheffler, M. Adsorbate-substrate and adsorbate-adsorbate interactions of Na and K adlayers on Al(111). *Phys. Rev. B* **46**, 16067–16080 (1992).
61. Makov, G. & Payne, M. C. Periodic boundary-conditions in ab-initio calculations. *Phys. Rev. B* **51**, 4014–4022 (1995).
62. Henkelman, G., Arnaldsson, A. & Jonsson, H. A fast and robust algorithm for Bader decomposition of charge density. *Comp. Mater. Sci.* **36**, 354–360 (2006).
63. Hapala, P. et al. Mechanism of high-resolution STM/AFM imaging with functionalized tips. *Phys. Rev. B* **90**, 085421 (2014).
64. Osawa, M., Ataka, K., Yoshii, K. & Nishikawa, Y. Surface-enhanced infrared-spectroscopy - the origin of the absorption enhancement and band selection rule in the infrared-spectra of molecules adsorbed on fine metal particles. *Appl Spectrosc* **47**, 1497–1502 (1993).

65. Tian, Y. et al Effect of ion-specific water structures at metal surfaces on hydrogen production. *Zenodo*. https://doi.org/10.5281/zenodo.13634826 (2024).

Acknowledgements

This work was supported by the National Key R&D Program of China under grants 2021YFA1400500; the National Natural Science Foundation of China under grants 92361302, 12250001, U22A20260, 11935002; the Strategic Priority Research Program of Chinese Academy of Sciences under grants XDB28000000 and XDB33000000; the Key R&D Program of Guangdong Province under grants 2020B010189001; the China Postdoctoral Science Foundation under grants 2022M720003 and 2023T160011; the Broad Agency Announcement (BAA) for Basic and Applied Scientific Research funded by the U.S. Army Research Laboratory (ARL); the U.S. Department of Defense (DoD); under Award Number W911NF1920065, by a grant from MISTI-China (Project No. 2244703). Y.J. acknowledges support from the New Cornerstone Science Foundation through the New Cornerstone Investigator Program and the XPLORER PRIZE. We are grateful for the computational resources provided by the TianHe-1A, TianHe II supercomputer, High-performance Computing Platform of Peking University.

Author contributions

Y.J. and Y.S.H. designed and supervised the project. Y.T. performed the STM/AFM measurements with D.G., J.H., B.H., and Y.Z. performed the SEIRAS and HER experiments. Y.S., D.C. and L.-M.X. performed ab initio DFT calculations and theoretical simulations of the AFM images. Y.T., B.H., Y.S., Y.Z., L.-M.X., E.-G.W., Y.S.H., and Y.J. analyzed the data. Y.T., B.H., Y.S., Y.Z., Y.S.H., and Y.J. wrote the manuscript with the inputs from all other authors. The manuscript reflects the contributions of all authors.

Competing interests

The authors declare no competing interests.

Additional information

Supplementary information The online version contains supplementary material available at https://doi.org/10.1038/s41467-024-52131-w.

Correspondence and requests for materials should be addressed to Ye Tian, Limei Xu, Yang Shao-Horn or Ying Jiang.

Peer review information *Nature Communications* thanks the anonymous reviewer(s) for their contribution to the peer review of this work. A peer review file is available.